

Optical properties and electronic structure of ZrB₁₂

J. Teyssier, A. B. Kuzmenko, D. van der Marel, and F. Marsiglio
*Département de Physique de la Matière Condensée, Université de Genève,
Quai Ernest-Ansermet 24, 1211 Genève 4, Switzerland*

A. B. Liashchenko, N. Shitsevalova, and V. Filippov
*Institute for Problems of Materials Science, National Academy of Sciences of Ukraine, 252680 Kiev, Ukraine
(Dated: November 11, 2018)*

We report optical (6 meV - 4 eV) properties of a boride superconductor ZrB₁₂ ($T_c = 6$ K) in the normal state from 20 to 300 K measured on high-quality single crystals by a combination of reflectivity and ellipsometry. The Drude plasma frequency and interband optical conductivity calculated by self-consistent full-potential LMTO method agree well with experimental data. The Eliashberg function $\alpha_{tr}^2 F(\omega)$ extracted from optical spectra features two peaks at about 25 and 80 meV, in agreement with specific heat data. The total coupling constant is $\lambda_{tr} = 1.0 \pm 0.35$. The low energy peak presumably corresponds to the displacement mode of Zr inside B_{24} cages, while the second one involves largely boron atoms. In addition to the usual narrowing of the Drude peak with cooling down, we observe an unexpected removal of about 10 % of the Drude spectral weight which is partially transferred to the region of the lowest-energy interband transition (~ 1 eV). This effect may be caused by the delocalization of the metal ion from the center of the B_{24} cluster.

PACS numbers: 74.70.Ad, 78.20.Ci, 78.30.-j

I. INTRODUCTION

Boron, like carbon, covalently bonds to itself, easily forming rigid three-dimensional clusters and networks as well as planes, chains and even nanotubes. The discovery of superconductivity in graphite-like MgB₂ at 40 K [1] has stimulated intense research of other superconducting boron phases, although they have so far shown quite modest transition temperatures. Zirconium dodecaboride ZrB₁₂ has one of the highest known $T_c \approx 6$ K among the binary borides except MgB₂. Even though the superconductivity there has been discovered almost 40 years ago [2], only recent progress in the single-crystal growth enabled its extensive studies.

In dodecaborides MB₁₂, boron atoms make up a three-dimensional network forming spacious B_{24} cages which accommodate metal ions. The isotope effect in ZrB₁₂ for zirconium [3] ($\beta \approx -0.32$) is much larger than for boron [4] ($\beta \approx -0.09$), pointing to a large contribution of lattice modes involving Zr atoms to the electron-phonon coupling responsible of superconductivity in ZrB₁₂. The inversion of specific heat measurements [5] gives a pronounced peak in the phonon density of states at about 15 meV, attributed to Zr vibrations in oversized boron cages. The coupling to this mode can also be enhanced by strong anharmonicity. The contribution to electron phonon coupling of this mode was also reported in Seebeck effect measurements [6].

Notably, significant controversy exists regarding the strength of the electron-phonon interaction. According to the McMillan formula, a weak-to-medium coupling $\lambda \approx 0.68$ provides the observed T_c , given the phonon mode frequency of 15 meV and a 'standard' value of the screened Coulomb potential $\mu^* \approx 0.1 - 0.15$ [7]. A weak coupling was confirmed by specific heat mea-

surements [5]. However, tunneling [8] and point-contact spectroscopy [7] yield $2\Delta_0/k_B T_c \approx 4.8$ suggesting a very strong coupling regime. This discrepancy between the results of surface and bulk probes has been ascribed to the surface-enhanced superconductivity in ZrB₁₂ [8, 9]. In principle, the value of λ can be also derived from the DC resistivity measurements, although this calculation relies on the unknown value of the plasma frequency.

Band structure calculation [10] shows that B 2p and Zr 4d states contribute almost equally to the density of states at the Fermi level. This makes ZrB₁₂ electronically very different from MgB₂, where Mg states have a vanishing contribution to the metallic and superconducting properties [11]. However, no experiments which can directly verify the prediction of the band theory, such as angle-resolved photoemission (ARPES), de Haas-van Alphen (dHvA) effect, have been done so far on this compound.

Optical spectroscopy that probes free carrier charge dynamics and provides experimental access to the plasma frequency, electron scattering and interband transitions, may help to clarify a number of existing uncertainties and test the predictions of the band calculations. By a combination of reflectivity and ellipsometry, we have obtained spectra of optical conductivity and dielectric function in the broad range of photon energies and frequencies. We concentrate on general optical fingerprints of the electronic structure of ZrB₁₂ in the normal state.

For comparison, we performed calculations of the band structure and corresponding optical properties. The electron-phonon coupling function $\alpha_{tr}^2 F(\omega)$ has been extracted from the fit of optical data and compared with thermodynamic and Raman measurements.

An unusual decrease of the Drude plasma frequency with cooling down is observed. By comparing with other

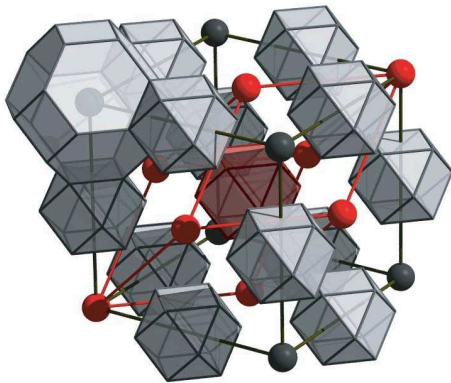


FIG. 1: (color on-line) Crystal structure of ZrB_{12} . The clusters B_{12} and B_{24} are displayed as polyhedrons. The unit cell containing 13 atoms is colored in red.

clustered compounds, we found that the delocalization of the metal ion (weakly bonded to the boron network) from the center of the boron cage could be at the origin of large changes in the electronic properties.

II. CRYSTAL STRUCTURE

ZrB_{12} crystallizes in the UB_{12} type structure [12] which can be viewed as a cubic rocksalt arrangement of Zr and B_{12} cuboctahedral clusters (Fig.1). For our discussion, it can be more convenient to represent this structure as a face centered cubic structure of Zr, surrounded by B_{24} cages.

III. OPTICAL EXPERIMENT AND RESULTS

Large single crystals of ZrB_{12} were grown using a high frequency induction zone furnace [13]. Optical measurements were performed on (001) surface with dimensions $4 \times 4 \text{ mm}^2$. The surface of this extremely hard material was polished using diamond abrasive disks with finest grain size of $0.1 \mu\text{m}$. In the photon energy range 0.8-4 eV, the complex dielectric function $\epsilon(\omega)$ was determined directly using spectroscopic ellipsometry at an incident angle of 60° . For photon energies between 6 meV and 0.8 eV, the reflectivity of the sample was measured using a Bruker 113 Fourier transform infrared spectrometer. For both ellipsometry and reflectivity experiments, the sample was mounted in a helium flow cryostat allowing measurements from room temperature down to 7 K. The reference was taken by *in situ* gold evaporation.

Fig.2a presents the real and imaginary parts of $\epsilon(\omega)$ measured by ellipsometry at selected temperatures. The reflectivity measured at low frequencies and extracted from the dielectric constant in the visible range, are plotted in Fig.2b.

In order to obtain the optical conductivity in the infrared region we used a variational routine [14] yielding

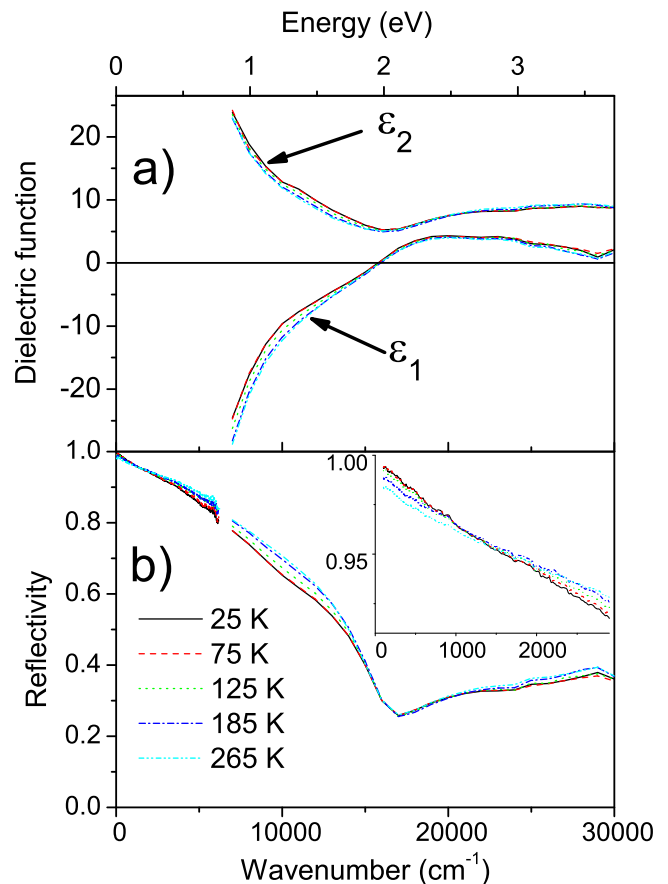


FIG. 2: (color on-line) a) Real and imaginary part of the dielectric function measured by ellipsometry. b) Reflectivity measured in the infrared and calculated from the dielectric constant at higher frequencies. Inset: low frequency region.

the Kramers-Kronig consistent dielectric function which reproduces all the fine details of the infrared reflectivity data while *simultaneously* fitting to the complex dielectric function in the visible and UV-range. This procedure anchors the phase of the infrared reflectivity to the phase at high energies measured with ellipsometry [15].

Fig. 3a shows the evolution of the optical conductivity with temperature. One can see a Drude-like peak that indicates a metallic behavior. The DC conductivity (σ_{DC}) [5, 7] plotted as symbols in the inset of Fig.3a, agrees reasonably well with the extrapolation of the optical data to zero frequency.

Fig.3b depicts the effective number of carriers

$$N_{\text{eff}}(\omega) = \frac{2mV_c}{\pi e^2} \int_0^\omega \sigma_1(\omega') d\omega' \quad (1)$$

where m is the free electron mass, e is the electron charge, $V_c=101.5 \text{ \AA}^3$ is the unit cell volume. We observe a transfer of spectral weight to low energy, which comes from the narrowing of the Drude peak. For higher energies (above 100 meV) an unusual decrease of up to 10% is observed. This will be discussed in section V C.

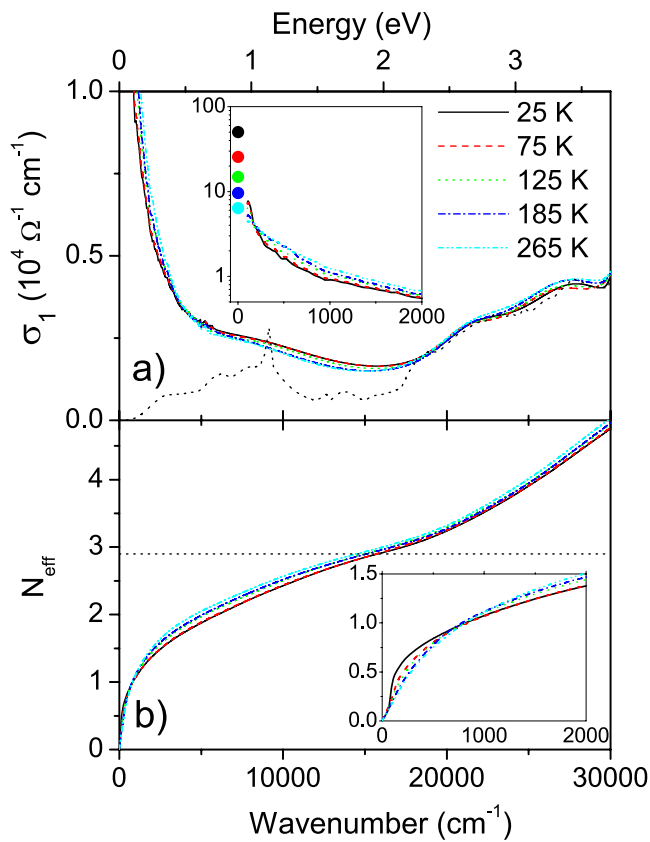


FIG. 3: (color on-line) a) Optical conductivity of ZrB_{12} at selected temperatures. Inset: low energy part, symbols represent σ_{DC} from [7]. The dotted line shows the interband conductivity from LDA calculation. b) Effective number of carriers per unit cell of 13 atoms, inset: low frequency part. The horizontal dotted line corresponds to the calculated plasma frequency of 6.3 eV.

IV. LDA CALCULATIONS

A. Band structure

The band structure was calculated for the unit cell containing 13 atoms. We used a full potential plane waves Linear Muffin-Tin Orbital (LMTO) program [16] within a Local Spin Density Approximation (LSDA) and Generalized Gradient Approximation (GGA) [17]. The band structure for high symmetry directions in the Brillouin Zone (BZ) is shown in Fig.4a. The density of states (DOS) calculated by the tetrahedron method is displayed in Fig.4b. It appears clearly that the main contribution to the DOS at the Fermi level comes from zirconium 4d and boron 2p states. The total DOS at the Fermi level $N(E_F) = 1.59 \text{ eV}^{-1}\text{cell}^{-1}$. $N(E_F)$ for zirconium d electron is $0.55 \text{ eV}^{-1}\text{cell}^{-1}$ and the one for p electrons of B_{12} clusters is $0.65 \text{ eV}^{-1}\text{cell}^{-1}$ which is in good agreement with a previous report [10].

Mapping the repartition of charges in a crystal is helpful to understand the chemical bonding. The calculated

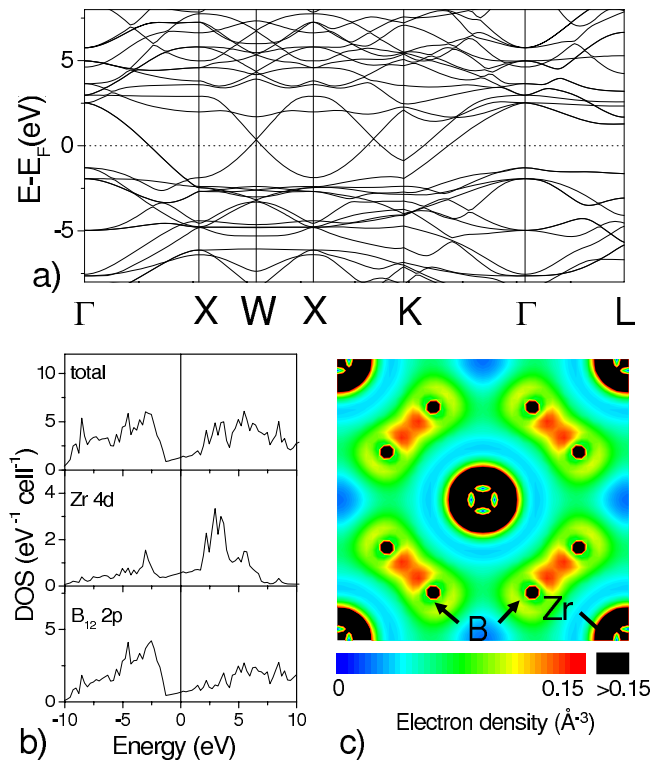


FIG. 4: (color on-line) a) Calculated band structure, b) partial density of states (PDOS) of ZrB_{12} . c) Charge density of in the a-b plane of the cubic cell.

charge density of valence electrons in the a-b plane of the cubic cell is displayed in Fig.4c. The high density between direct neighbor boron atoms indicates a strong covalent bonding while the ion in the middle of the B_{24} cage (Zr in our case) is weakly bonded to the boron skeleton. This has strong consequences on vibration modes in the crystal and may explain the presence of a very low frequency phonon ($\sim 15 \text{ meV}$) associated with a displacement of the zirconium atom in the B_{24} cage.

Fig.5a shows the Fermi surface in the first Brillouin zone. The sheet centered at X (marked in red in Fig.5) has electron character while the network centered on the Γ point (marked in blue in Fig.5) is of hole character. The two sheets are touching at point *a* along the Γ X direction. In contrast to MgB_2 , which exhibits a strongly anisotropic Fermi surface composed of different sheets with very different character of carriers, the Fermi surface in ZrB_{12} is much more isotropic.

B. Optical properties

The LDA band structure allows us to calculate the optical parameters. The interband contribution to the real part of the optical conductivity can be deduced from

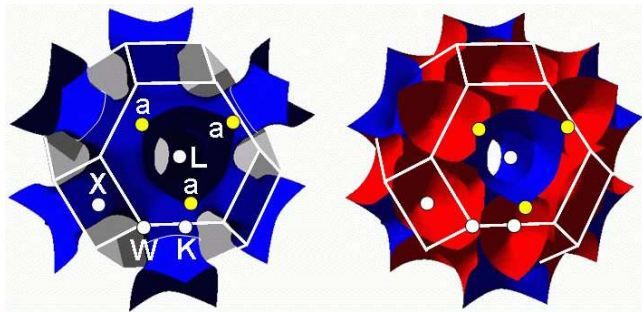


FIG. 5: (color on-line) Fermi surface of ZrB_{12} containing two sheets: a hole-like network (blue) and electron-like closed surfaces (red). In the left figure only the first sheet is displayed for clarity. The points of tangential contact between the two sheets are designated by symbol a .

the equation:

$$\sigma_1(\omega) = \frac{e^2}{12\pi^2 m^2 \omega} \sum_{f,i} \int_{BZ} d^3k |P_{fi}|^2 \delta[E_f(k) - E_i(k) - \hbar\omega]$$

$$P_{fi} = \frac{\hbar}{i} \langle f | \nabla | i \rangle$$

Here, $E_i(k)$ and $E_f(k)$ are the energies of the initial (occupied) and final (empty) states, respectively. k is the wave vector inside the BZ where the transition $E_i(k) \rightarrow E_f(k)$ occurs. Only direct transitions are taken into account. The calculated optical conductivity is shown as the dotted line in Fig.3a together with experimental curves. At frequencies above 2 eV a very good agreement is observed. At lower frequencies, the experimental curves are systematically higher likely due to the tail of the Drude peak.

The plasma frequency was computed through integration on the Fermi surface :

$$\Omega_{p,LDA}^2 = \frac{e^2}{12\pi^2} \int_{FS} v_f dS \quad (2)$$

where v_f is the Fermi velocity. We found a value $\Omega_{p,LDA} = 6.3$ eV which corresponds to $N_{eff} \approx 2.9$ (dotted line in Fig.3b). The experimental value of $N_{eff}(\omega)$ reaches this level at about 2 eV where the experimental optical conductivity (Fig.3a) shows a minimum. This indicates that the calculated plasma frequency is close to the experimental one.

V. ANALYSIS AND DISCUSSION

A. Extended drude analysis

Fig.6 shows the frequency dependence of the mass renormalization $m^*(\omega)/m_b$ (m_b is the band mass) and the

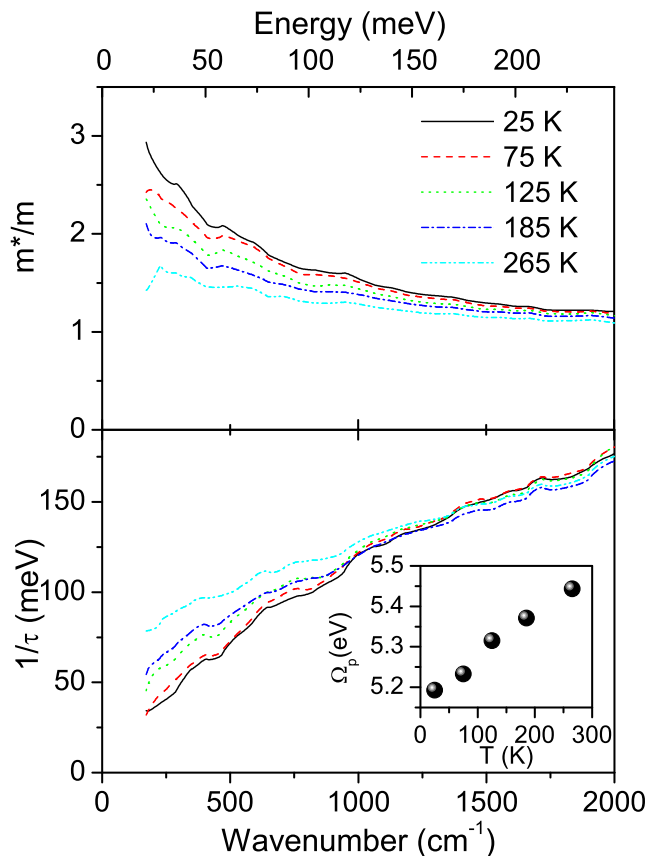


FIG. 6: (color on-line) Extended Drude analysis of the optical conductivity of ZrB_{12} for different temperatures. Inset shows the T dependence of the plasma frequency used to calculate m^*/m and $1/\tau$.

scattering rate $1/\tau(\omega)$ obtained by the extended Drude formalism:

$$\frac{m^*(\omega)}{m_b} = -\frac{\Omega_p^2}{4\pi\omega} \text{Im} \left(\frac{1}{\sigma(\omega)} \right) \quad (3)$$

$$\frac{1}{\tau(\omega)} = \frac{\Omega_p^2}{4\pi} \text{Re} \left(\frac{1}{\sigma(\omega)} \right) \quad (4)$$

The plasma frequency Ω_p was obtained at each temperature by integration of optical conductivity from zero to 0.74 eV (6000 cm^{-1}) (inset in Fig.6). This cutoff frequency was chosen such that Ω_p is close to the plasma frequency obtained using the fitting procedure (fit 3) described below. The temperature dependence of Ω_p is too large to be neglected as it is usually done.

At low frequencies, the decrease of the scattering rate with cooling down indicates a narrowing of the Drude peak. The strong frequency dependence below 100 meV of $1/\tau(\omega)$ and $m^*(\omega)/m_b$ indicates a significant electron-boson, presumably electron-phonon interaction.

B. Electron-phonon coupling

The signature of electron-phonon interaction shown by the extended Drude analysis makes the simple Drude model inapplicable to describe the low frequency region. Therefore, we adopted the following model for the dielectric function:

$$\epsilon(\omega) = \epsilon_\infty - \frac{\Omega_p^2}{\omega[\omega + iM(\omega, T)]} + \sum_j \frac{\Omega_{p,j}^2}{\omega_{0,j}^2 - \omega^2 - i\omega\gamma_j} \quad (5)$$

ϵ_∞ represents the contribution of core electrons, the second and the third terms describe free carriers and interband contributions respectively. The latter is taken to be a sum of Lorentzians with adjustable parameters. The frequency dependent scattering of the free carriers is expressed via the memory function:

$$M(\omega, T) = \gamma_{imp} - 2i \int_0^\infty d\Omega \alpha_{tr}^2 F(\Omega) K \left(\frac{\omega}{2\pi T}, \frac{\Omega}{2\pi T} \right) \quad (6)$$

where γ_{imp} is the impurity scattering rate and $\alpha_{tr}^2 F(\Omega)$ is the transport Eliashberg function. The kernel K is [18]:

$$K(x, y) = \frac{i}{y} + \left\{ \frac{y-x}{x} [\Psi(1-ix+iy) - \Psi(1+iy)] \right\} - \{y \rightarrow -y\} \quad (7)$$

where $\Psi(x)$ is the digamma function.

The reflectivity at normal incidence is:

$$R(\omega) = \left| \frac{\sqrt{\epsilon(\omega)} - 1}{\sqrt{\epsilon(\omega)} + 1} \right|^2 \quad (8)$$

We fit simultaneously $R(\omega)$ at low frequencies and both $\epsilon_1(\omega)$ and $\epsilon_2(\omega)$ at high frequencies.

As a starting point, we used $\alpha^2 F(\Omega)$ deduced from specific heat and resistivity measurements (neglecting the difference between isotropic $\alpha^2 F(\Omega)$ and transport $\alpha_{tr}^2 F(\Omega)$) [5] and adjusted all other parameters (fit 1: solid red curve in Fig.7a). This function (solid curve in Fig.8) has two peaks around 12 meV and 60 meV and gives $\lambda = 0.68$. A clear improvement of the fit quality was achieved compared to one with a single Drude peak (dashed dotted curve) with frequency independent scattering rate. The reflectivity curve is within absolute reflectivity error bars of 0.5%. This means that optical data are consistent with the mentioned value of the coupling constant and the observed T_c [5, 7].

It is also important to determine the spread of parameters consistent with optical data alone. It is known that the extraction of $\alpha^2 F(\Omega)$ from optical data is an ill-posed problem [19, 20, 21] which means that fine details cannot be extracted. We model the Eliashberg function as a superposition of Dirac peaks:

$$\alpha_{tr}^2 F(\Omega) = \sum_k A_k \delta(\Omega - x_k) \quad (9)$$

TABLE I: Set of parameters used in fit 2 and fit 3. In fit 3, the Lorentzian L_1 is split into three different ones.

		Fit 2	Fit 3		
			L_{1a}	L_{1b}	L_{1c}
	ϵ_∞	3.33	3.28		
	Ω_p (eV)	5.5	5.2		
	γ_{imp} (meV)	33	28		
Low Energy (L_1)	ω_o (eV)	1	0.32	0.74	1.21
	Ω_p (eV)	4.6	1.03	0.50	5.76
	γ (eV)	1.8	0.30	0.15	2.75
L_2	ω_o (eV)	2.6	2.8		
	Ω_p (eV)	1.9	2.1		
	γ (eV)	0.6	0.5		
L_3	ω_o (eV)	3.3	3.4		
	Ω_p (eV)	4.7	4.1		
	γ (eV)	1.3	1.0		
L_4	ω_o (eV)	4.8	4.7		
	Ω_p (eV)	8.3	7.9		
	γ (eV)	1.9	1.6		

and treat A_k and x_k as free parameters. We did not succeed to obtain a reasonable fit with a single mode even using some gaussian broadening within 10 meV but two peaks are sufficient to reproduce the shape of experimental curves. The central frequencies were found to be $x_1=208 \pm 19 \text{ cm}^{-1}$ and $x_2=602 \pm 128 \text{ cm}^{-1}$. The weights are $A_1=83 \pm 21 \text{ cm}^{-1}$ and $A_2=94 \pm 35 \text{ cm}^{-1}$ respectively. The electron-phonon coupling constant can be derived from the parameters of the fit by the relation:

$$\lambda_{tr} = 2 \int_0^\infty \frac{d\Omega \alpha_{tr}^2 F(\Omega)}{\Omega} = 2 \sum_k \frac{A_k}{x_k} \quad (10)$$

In our case, this ratio leads to a partial coupling constant $\lambda_{tr,1}=0.82 \pm 0.28$ for the mode at x_1 and $\lambda_{tr,2}=0.18 \pm 0.10$ for the mode at x_2 . The total $\lambda_{tr}=1.00 \pm 0.35$. The other parameters of the fit are displayed in table I. The reflectivity corresponding to this fit (fit 2) is displayed as the dotted (green) curve in Fig.7a.

The low frequency mode can be logically assigned to the vibration of weakly bounded zirconium ion inside B_{24} cages, although the ab-initio calculation of the phonon structure is needed to substantiate this assignment. The high frequency mode presumably corresponds to a rigid boron network vibration; a situation similar to intercalated fullerenes and other clustered covalent structures.

The error bars of x_k and A_k are quite large because of a significant numerical fit correlation between the lowest energy interband transition and the parameters of the oscillator ($L1$ in table I) and those of $\alpha_{tr}^2 F(\Omega)$. In other words, it is difficult to decouple the effects of low energy interband transition and electron-phonon interaction on the optical conductivity. Therefore we performed another fit (fit 3) where the interband contribution was modeled (parameters in table I) to match the one of the interband optical conductivity calculated by LDA (solid line in Fig.7b). The presence of sharp structures slightly worsens the quality of the fit. The

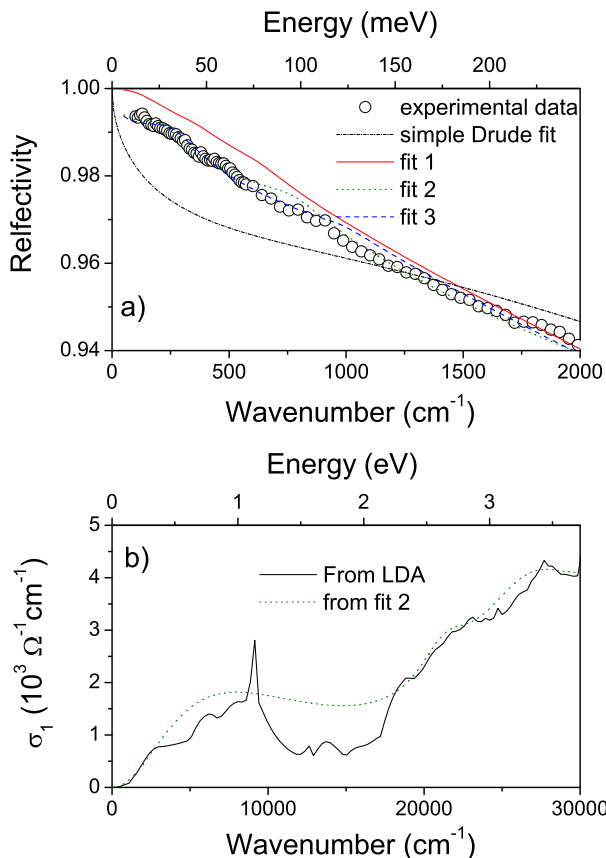


FIG. 7: a) Different fits of reflectivity at 25K. dash-dotted line is a fit with a single Drude peak. Fit 1 with $\alpha^2 F(\Omega)$ from [5] (solid red curve). Fit 2 and 3 $\alpha_{tr}^2 F(\Omega)$ was adjustable as described in the text. b) Interband contribution to optical conductivity calculated from LDA (solid curve) and obtained from the Fit 3 as described in the text.

low energy mode of $\alpha_{tr}^2 F(\Omega)$ is almost unchanged by this procedure ($x_1=227 \text{ cm}^{-1}$, $A_1=106 \text{ cm}^{-1}$ and $\lambda_{tr1}=0.93$) but the second mode tends to shift to higher frequencies ($x_2=1003 \text{ cm}^{-1}$, $A_2=190 \text{ cm}^{-1}$ and $\lambda_{tr2}=0.38$) and the total coupling constant becomes $\lambda_{tr}=1.3$. The reflectivity corresponding to fit 3 is plotted as a dashed blue curve in Fig.7a.

The central frequencies x_k and partial electron-phonon constants λ_k are shown as symbols in Fig.8 for fit 2 (circles) and fit 3 (squares) described above. The Eliashberg function from [5] used in fit 1 is plotted as a solid curve. Central frequencies of the phonons are larger than those derived from specific heat and resistivity measurements [5] (140 cm^{-1} and 420 cm^{-1}) (Fig. 8).

A more traditional way to extract $\alpha_{tr}^2 F(\Omega)$ from optical conductivity is to use directly the inversion formula[19, 22]:

$$\alpha_{tr}^2 F(\omega) = \frac{1}{2\pi} \frac{\Omega_p^2}{4\pi} \frac{d^2}{d\omega^2} \left(\omega \text{Re} \frac{1}{\sigma(\omega)} \right) \quad (11)$$

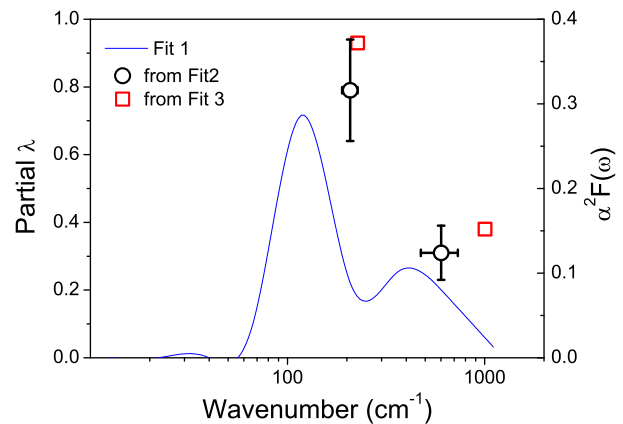


FIG. 8: (color online) The solid curve (fit 1) corresponds to $\alpha^2 F(\Omega)$ from [5]. Central phonon frequencies and partial coupling constant extracted from fit of optical data with fit 2 (circles) and fit 3 (squares) procedures as described in the text.

One can also calculate the integrated coupling constant:

$$\lambda_{tr,int}(\omega) = 2 \int_0^\omega \frac{d\Omega \alpha_{tr}^2 F(\Omega)}{\Omega} \quad (12)$$

Taking the frequency derivative twice requires heavy spectral smoothing of optical data. The result of inversion is given in Fig.9 for different frequency smoothing windows. The robust features in $\alpha_{tr}^2 F(\omega)$ are the peaks at about 250 cm^{-1} and 900 cm^{-1} , in good agreement with the results obtained by fitting procedures described above. Since Eq.(11) assumes the absence of low energy interband transition, in our case some spurious features in $\alpha_{tr}^2 F(\omega)$ may appear at frequencies above $\sim 1000 \text{ cm}^{-1}$. Even though smoothing has a significant influence on the shape of $\alpha_{tr}^2 F(\omega)$, all curves $\lambda_{tr,int}(\omega)$ lie almost on top of each other and give a value of about 1.1 around 1000 cm^{-1} . Summarizing the results of all previously described approaches to extract $\alpha_{tr}^2 F(\omega)$, we obtained $\lambda_{tr} = 1.0 \pm 0.3$. This value indicates a medium to strong coupling in ZrB_{12} .

C. Temperature dependence of Drude spectral weight

The plasma frequency Ω_p at 25 K, obtained from different fits (Table I) is 5.2-5.5 eV. The uncertainty is coming from the fact that interband contributions, which can not be separated unambiguously from the Drude peak. This value is slightly lower than the one calculated by LDA (6.3 eV). However this agreement is good and it suggests that LDA describes well the conduction bands near the Fermi surface. The temperature dependence of the plasma frequency though appears to be anomalous. As it was mentioned above, the integrated number of carriers decreases for energies above 100 meV when temperature is decreased. This is shown in Fig.10 where we plot N_{eff}

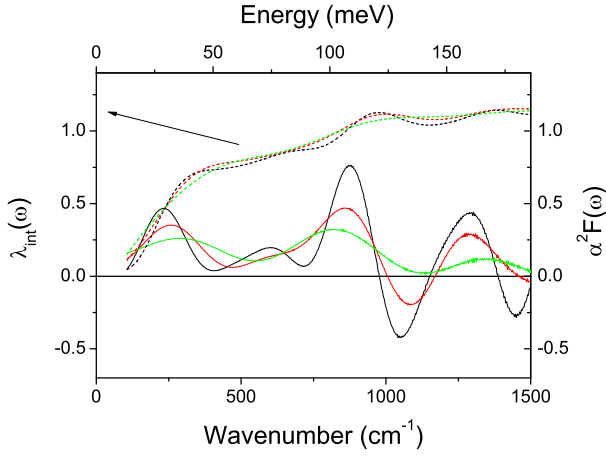


FIG. 9: (color online) $\alpha_{tr}^2 F(\Omega)$ obtained using Eq.(11) at $T=25$ K (solid curves) and integrated coupling constant $\lambda_{tr,int}(\omega)$ (dashed curves) for different smoothing windows.

as a function of temperature normalized by its value at 20 K for selected cutoff frequencies. The effect is maximal (about 10%) at around 0.7 eV. Normally, the narrowing of the Drude peak with a temperature independent plasma frequency results in a slight (1-2%) increase of N_{eff} at frequencies 0.5-1 eV. In our case one has to assume that the plasma frequency decreases with cooling down. On the other hand, spectral weight is almost recovered at around 2 eV which is due to the fact that it is transferred from the low frequency range to the region between 0.5 and 2 eV (Fig.3).

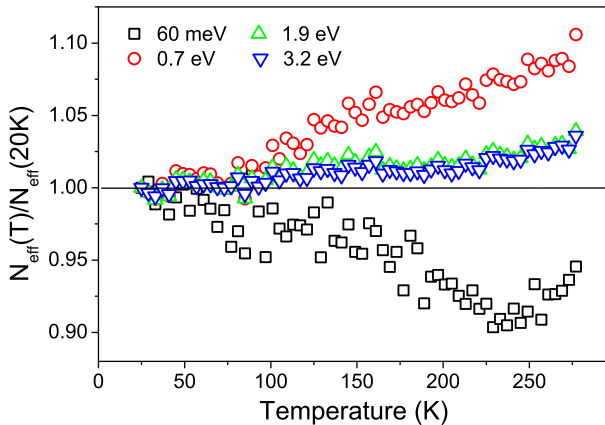


FIG. 10: (Color online) Temperature dependence of relative effective number of carriers for different cutoff energies.

We do not have a definitive explanation of this effect. In order to check the direct effect of temperature on the band structure, we have performed LDA calculations at finite temperatures by adding a Fermi-Dirac distribution for the bands filling in the self consistent calculation. The thermal expansion was also taken into account using data from Ref.5. We found that the calculated plasma frequency decreases around 0.4% with increasing tem-

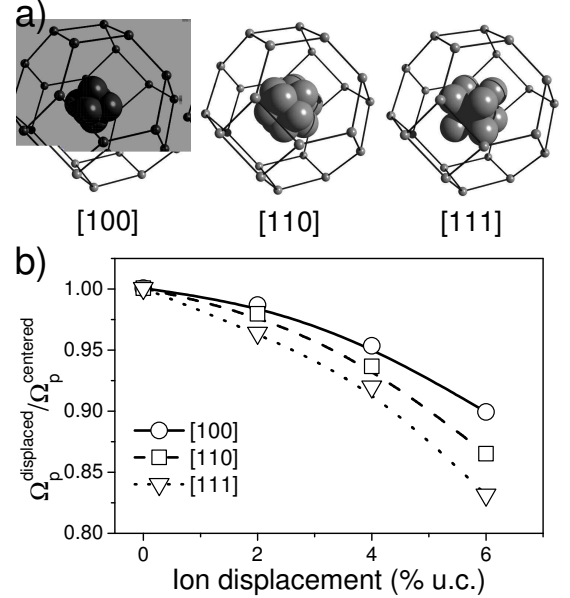


FIG. 11: a) Representation of displacement directions in the B_{24} cage. b) Plasma frequency versus ionic displacement along [100], [110] and [111] directions.

perature from 0 K to 600 K. Both sign and amplitude of the change in the calculated plasma frequency cannot explain the experimental observations. The spectral weight due to interband transitions has also been calculated and found to be almost temperature independent. Therefore a decrease of 10% of the spectral weight is so big that it likely results from a significant change of the electronic band structure.

One can speculate that a certain structural instability is due to the ability of zirconium atoms to move almost freely in spacious boron cages. According to Ref.23, a displacement of the metal ion in the B_{24} cage of about 5% of the unit cell is responsible for the symmetry breaking which makes low frequency Zr mode Raman-active. We have therefore calculated the band structure and the plasma frequency as a function of displacement of the metal ion in the directions [100],[110] and [111]. The delocalization configurations are sketched in Fig.11a.

Electron states at the Fermi surface are equally coming from Zr atoms and B_{12} cluster (Fig.4b). Therefore the highest plasma frequency is obtained when Zr ion is in the center of the B_{24} cluster. The plasma frequency decrease will be more pronounced when Zr shifts towards a region with lower charge density (Fig.11b).

Such an anomalously large atomic displacement has already been observed in clathrate-type systems that present a similar cluster structure [24, 25]. In these compounds, the displacement of an ion located in the middle of a cage is strongly anisotropic and can be described by a fractionally occupied split site. It was also found that this atomic disorder was present from room temperature

down to 10K.

In the picture of a multiple well potential, the delocalization due to thermal excitation tends to center the ion in the middle of the cage. At low temperature, the ion is located in the bottom of the well out of the central position. Further structural investigations are necessary to elucidate the relevancy of this or other scenarios in dodecaborides. This kind of spectral weight transfer is also predicted by the model where the charge carriers are small polarons[26]. While keeping in mind that they have been derived for a low charge carrier density, the observed direction of the spectral weight transfer agrees with those models.

VI. CONCLUSIONS

In this work, optical properties of zirconium dodecaboride have been studied as a function of temperature. We found that LDA theory predicts correctly interband optical conductivity and free electron plasma frequency.

ZrB₁₂ appears to be a good metal with a bare plasma frequency of about 5.5 eV. The Eliashberg function $\alpha_{tr}^2 F(\Omega)$ was extracted by two methods giving consistent results. Two peaks were found in $\alpha_{tr}^2 F(\Omega)$ at about 200 and 1000 cm⁻¹ which is consistent with specific heat measurements [5]. A medium to high electron-phonon coupling regime is found with $\lambda_{tr} \simeq 1.0$ in agreement with a high ratio $2\Delta_o/kT_c = 4.8$ from tunneling measurements

[8]. The low frequency peak that likely corresponds to a vibration mode of zirconium in boron cages is the main contributor to the coupling constant.

However, this compound shows deviations from conventional metallic behavior. Namely, a significant anomaly in the temperature evolution of the integrated spectral weight was observed. About 10% of the spectral weight is removed from the Drude peak and transferred to the region of low energy interband transitions. The origin of this anomaly has not been clearly identified. However, our simulation of the impact of the delocalization of the metal ion in the boron cages shows that it could be responsible for the large change in the plasma frequency.

VII. ACKNOWLEDGMENTS

The authors would like to thank Rolf Lortz and Alain Junod for fruitful exchanges. This work was supported by the Swiss National Science Foundation through the National Center of Competence in Research Materials with Novel Electronic Properties-MaNEP. FM greatly appreciates the hospitality of the Department of Condensed Matter Physics at the University of Geneva. This work was supported in part by the Natural Sciences and Engineering Research Council of Canada (NSERC), by ICORE (Alberta), and by the Canadian Institute for Advanced Research (CIAR).

-
- [1] J. Nagamatsu, N. Nakagawa, T. Muranaka, Y. Zenitani, and J. Akimitsu, *Nature* **410**, 63 (2001).
- [2] B. T. Matthias, T. H. Geballe, K. Andres, E. Corenzwit, G. W. Hull, and J. P. Maita, *Science* **159**, 530 (1968).
- [3] C. W. Chu and H. H. Hill, *Science* **159**, 1227 (1968).
- [4] Z. Fisk, A. C. Lawson, B. T. Matthias, and E. Corenzwit, *Phys. Lett.* **37A**, 251 (1971).
- [5] R. Lortz, Y. Wang, S. Abe, V. Gasparov, Y. B. Paderno, V. Filippov, and A. Junod, *Phys. Rev. B* **72**, 024547 (2005).
- [6] V. Glushkov, M. Ignatov, S. Demishev, V. Filippov, K. Flachbart, T. Ishchenko, A. Kuznetsov, N. Samarin, N. Shitsevalova, and N. Sluchanko, *Phys. Stat. Sol. (b)* **243**, 72 (2006).
- [7] D. Daghero, R. S. Gonnelli, G. A. Ummarino, A. Calzolari, V. Dellarocca, V. A. Stepanov, V. B. Filippov, and Y. B. Paderno, *Supercond. Sci. Technol.* **17**, 250 (2004).
- [8] M. I. Tsindlekht, G. I. Leviev, I. Asulin, A. Sharoni, O. Millo, I. Felner, Y. B. Paderno, and V. B. F. M. A. Belogolovskii, *Phys. Rev. B* **69**, 212508 (2004).
- [9] R. Khasanov, D. D. Castro, M. Belogolovskii, Y. Paderno, V. Filippov, R. Brüttsch, and H. Keller, *Phys. Rev. B* **72**, 224509 (2005).
- [10] I. R. Shein and A. L. Ivanovskii, *Physics of the Solid State* **45**, 1429 (2003).
- [11] J. Kortus, I. I. Mazin, K. D. Belashchenko, V. P. Antropov, and L. L. Boyer, *Phys. Rev. Lett.* **86**, 4656 (2001).
- [12] A. Leithe-Jasper, A. Sato, and T. Tanaka, *Z. Kristallogr.* **217**, 319 (2002).
- [13] Y. B. Paderno, A. B. Liashchenko, V. B. Filippov, and A. V. Dukhnenko, *Proc. Int. Conf. on science for materials in the frontier of the Centuries: Advantages and Challenges IPMS NASU Kiev* p. 347 (2002).
- [14] A. B. Kuzmenko, *Rev. Sci. Instr.* **76**, 83108 (2005).
- [15] I. Bosovic, *Phys. Rev. B* **42**, 1964 (1990).
- [16] S. Y. Savrasov, *Phys. Rev. B* **54**, 16470 (1996).
- [17] J. P. Perdew, K. Burke, and M. Ernzerhof, *Phys. Rev. Lett.* **77**, 3865 (1996).
- [18] O. Dolgov and S. Shulga, *J. Supercond.* **8**, 611 (1995).
- [19] F. Marsiglio, *J. of superconductivity* **12**, 163 (1999).
- [20] S. Shulga, *Kluwer Academic Publishers, Dordrecht*, 323-360 (2001), cond-mat/0101243.
- [21] S. V. Dordevic, C. C. Homes, J. J. Tu, T. Valla, M. Strongin, P. D. Johnson, G. D. Gu and D. N. Basov, *Phys. Rev. B* **71**, 104529 (2005).
- [22] F. Marsiglio, T. Startseva, and J. Carbotte, *Phys. Lett. A* **245**, 172 (1998).
- [23] H. Werheit, Y. Paderno, V. Filippov, V. Paderno, A. Pietraszko, M. Armbrüster, and U. Schwarz, *J. of Solid State Chem. (to be published)* (2006).
- [24] B. Chakoumakos, B. Sales, D. Mandrus, and G. Nolas, *J. Alloys and Compounds* **296**, 80 (2000).
- [25] B. Chakoumakos, B. Sales, and D. Mandrus, *J. Alloys and Compounds* **322**, 127 (2001).
- [26] D. Emin, *Phys. Rev. B* **48**, 13691 (1993).